

Radical-induced Low-field Relaxation and Thermal Mixing in Pyruvic Acid

Hana Kouřilová,^{1,*} Michael Jurkutat,^{1,†} David Peat,² Karel Kouřil,¹ Alixander S. Khan,² Anthony J. Horsewill,² James F. MacDonald,² John Owers-Bradley,² and Benno Meier^{1,3,‡}

¹*Institute of Biological Interfaces 4, Karlsruhe Institute of Technology, Germany*

²*School of Physics and Astronomy, University of Nottingham, Nottingham, NG7 2RD, UK*

³*Institute of Physical Chemistry, Karlsruhe Institute of Technology, Germany*

(Dated: February 14, 2022)

In dynamic nuclear polarization, polarization is transferred from electron to nuclear spins at low temperatures. So far, it is not possible to predict the relaxation of hyperpolarized solids, and applications are developed largely by trial and error. Here, we study the low-field nuclear spin relaxation in pyruvic acid, doped with trityl. We find that, at low fields, the relaxation time constants for both ¹³C and ¹H scale linearly with the applied field. We model the data using a thermodynamic approach, in which heat is transferred via triple-spin-flips involving two electron spins and one nuclear spin. The triple-spin-flip rate is calculated from first principles using a formalism developed by Wenckebach. The heat capacity of the Non-Zeeman reservoir is determined from the ¹H relaxation data at intermediate fields, which leads to a parameter-free, yet nearly quantitative description of the observed ¹H relaxation rates from 5 mT to 2 T. The observed ¹³C relaxation is consistent with the formalism, provided that the direct energy exchange between the ¹H and ¹³C reservoirs, and the diffusion barrier are accounted for at low and high fields, respectively. The formalism also describes the observed electron-mediated ¹H-¹³C thermal mixing.

INTRODUCTION

Nuclear magnetic resonance (NMR) and magnetic resonance imaging are powerful non-invasive techniques used to study the structure and dynamics of matter. At room temperature, however, only 1 in 100,000 ¹H spins contributes to the NMR signal in a 3 T MRI scanner.

Dissolution-dynamic nuclear polarization (D-DNP), first reported by Ardenkjær-Larsen and co-workers^{1–4}, can alleviate the low sensitivity of magnetic resonance. In D-DNP nuclear spins are polarized to a high degree by coupling them to nearly fully polarized electron spins using microwave irradiation, typically at a temperature of 1 K. The sample is then dissolved with hot solvent, yielding a solution containing highly polarized molecules, that is transferred to a secondary apparatus for detection. D-DNP has enabled the *in vivo* observation of human metabolism using magnetic resonance imaging^{5–8}.

We have recently demonstrated a slightly different scheme, named bullet-DNP, where the hyperpolarized solid is transferred to the secondary apparatus within less than 100 ms, and dissolved only near the point of use^{9,10}. This scheme is fast and scalable towards small solvent volumes as they are used in NMR spectroscopy¹¹. It may be useful also for the transfer of hyperpolarized substances where the T_1 in liquid-state is short, as is the case for high- γ nuclei and larger molecules.

Here, we study the low-field relaxation of solid pyruvic acid, doped with the narrow-band OX063 trityl radical. Surprisingly, the field-dependent low-temperature relaxation behaviour of this widely used material has never previously been studied.

At low fields, the relaxation time constants of protons and carbons, measured using field-cycling NMR, increase linearly with the applied magnetic field. The data are analysed using a thermodynamic spin tempera-

ture model as first described by Provotorov.^{12–14} In this model, the nuclear Zeeman spin reservoirs are coupled to the electron Non-Zeeman reservoir via energy-conserving triple-spin flips (TSF), in which a nuclear spin flip and an electron-electron flip-flop occur simultaneously.¹⁵ We calculate the TSF rate from first principles,^{16,17} using only a Monte-Carlo based estimate of the spectrum of electron spin-spin interactions¹⁸, and the inhomogeneous EPR linewidth, which is known from electron paramagnetic resonance (EPR) data.¹⁹ We use the nuclear relaxation data and the TSF rate to derive a correction of the Monte Carlo based spin-spin spectrum, which leads to nearly quantitative agreement between the model and the measured relaxation rates for protons over two orders of magnitude in magnetic field.

The model may also be used to estimate the field-dependent carbon relaxation rate. Here, we find that the predicted ¹³C relaxation rates are underestimated at low fields, and overestimated at high fields. The discrepancy at low field is attributed to a faster direct carbon-proton cross-relaxation process due to trityl. The discrepancy at high field is discussed in terms of a field-dependent polarization transfer across the spin diffusion barrier.³¹.

We further show that the coupling of the electron NZ reservoir to proton and carbon spins gives rise to an efficient proton-carbon polarization transfer at intermediate fields of the order of 100 mT.

Spin reservoirs, temperature and energy exchange

In Provotorov's theory, relaxation is modelled as a flow of heat between different spin reservoirs and the lattice.¹⁴ The different spin reservoirs correspond to commuting terms in the spin Hamiltonian of the system. Following a perturbation, each reservoir quickly achieves an

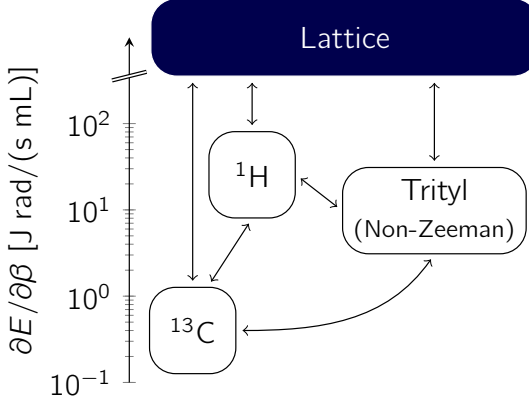


Figure 1. Heat capacities of the ^1H and ^{13}C nuclear Zeeman reservoirs (for pyruvic acid and a magnetic field strength of 20 mT), and the trityl Non-Zeeman reservoir. All reservoirs exhibit field-dependent couplings to each other and the lattice.

internal equilibrium, which is described by a spin temperature. The heat capacities of each reservoir are obtained as derivatives of their energy with respect to inverse temperature $\beta = 1/k_B T$.¹⁴ The relevant reservoirs for the system discussed here are the nuclear Zeeman reservoirs, and the electron non-Zeeman reservoir. These three reservoirs couple to each other and the lattice as sketched in Fig. 1. The electron Zeeman reservoir cannot couple to any of these reservoirs and is ignored. Likewise, the nuclear non-Zeeman reservoirs are ignored due to their small heat capacity.

For the nuclear Zeeman reservoirs with energies E_i , with $i \in \{^1\text{H}, ^{13}\text{C}\}$, and the electron Non-Zeeman reservoir with E_{NZ} , the heat capacities are, respectively,

$$C_i = \frac{\partial E_i}{\partial \beta_i} = \hbar \gamma_i^2 B^2 N_i \frac{I(I+1)}{3} \quad (1)$$

$$C_{\text{NZ}} = \frac{\partial E_{\text{NZ}}}{\partial \beta_{\text{NZ}}} = \hbar \gamma_S^2 H_L^2 N_S \frac{S(S+1)}{3}, \quad (2)$$

where B is the applied magnetic field, γ_i is the gyromagnetic ratio and N_i is the concentration of the respective nuclear spins. The local field H_L due to spin-spin interactions is $\gamma_S^2 H_L^2 = (5/3)M_2$, where M_2 is the second moment of the dipolar EPR line, and $I = S = 1/2$ is the spin of the involved species.¹⁴ The Zeeman heat capacities scale quadratically with the applied field, whereas the Non-Zeeman heat capacity is field-independent. Therefore, as the field is lowered, the electron Non-Zeeman heat capacity becomes larger than the heat capacities of the carbon and, eventually, the proton Zeeman reservoir.

The heat exchange of the three reservoirs with each other and the lattice, depicted in Fig. 1, is described by a set of three linear differential equations.

$$\begin{aligned} \frac{\partial \beta_{\text{H}}}{\partial t} = & -\frac{1}{\tau_{\text{NZ-H}}} \frac{C_{\text{NZ}}}{C_{\text{H}}} (\beta_{\text{H}} - \beta_{\text{NZ}}) \\ & -\frac{1}{\tau_{\text{H-C}}} \frac{C_{\text{C}}}{C_{\text{H}}} (\beta_{\text{H}} - \beta_{\text{C}}) - \frac{\beta_{\text{H}}}{T_{1,\text{H}}} \end{aligned} \quad (3)$$

$$\begin{aligned} \frac{\partial \beta_{\text{C}}}{\partial t} = & -\frac{1}{\tau_{\text{NZ-C}}} \frac{C_{\text{NZ}}}{C_{\text{C}}} (\beta_{\text{C}} - \beta_{\text{NZ}}) \\ & +\frac{1}{\tau_{\text{H-C}}} (\beta_{\text{H}} - \beta_{\text{C}}) - \frac{\beta_{\text{C}}}{T_{1,\text{C}}} \end{aligned} \quad (4)$$

$$\begin{aligned} \frac{\partial \beta_{\text{NZ}}}{\partial t} = & +\frac{1}{\tau_{\text{NZ-H}}} (\beta_{\text{H}} - \beta_{\text{NZ}}) + \frac{1}{\tau_{\text{NZ-C}}} (\beta_{\text{C}} - \beta_{\text{NZ}}) \\ & -\frac{\beta_{\text{NZ}}}{T_{1,\text{S}}} \end{aligned} \quad (5)$$

Here, $\beta_i = \beta'_i - \beta_{\text{L}}$, with $i \in [\text{H}, \text{C}, \text{NZ}]$ is the difference of the respective reservoir's inverse temperature $\beta'_i = 1/(k_B T_i)$ and the inverse lattice temperature, β_{L} . The nuclear reservoirs with inverse temperatures β_{H} and β_{C} couple to the Non-Zeeman reservoir, each other, and the lattice, while vice versa the Non-Zeeman reservoir with inverse temperature β_{NZ} couples to the two nuclear reservoirs and the lattice.

In neat pyruvic acid, the spin-lattice relaxation time constants $T_{1,\text{H/C}}$, can be measured directly, with the exception of ^{13}C at fields below 10 mT where the carbon relaxation is due to direct exchange with the proton reservoir, $1/\tau_{\text{H-C}} > 0$. The electronic $1/T_{1,\text{S}}$ of doped PA is known from earlier work by Lumata et al.¹⁹

The presence of trityl then is expected to cause additional relaxation of both protons and carbons via the Non-Zeeman reservoir. This relaxation may be modelled quantitatively, if the (field-independent) heat capacity of the Non-Zeeman reservoir, and the (field-dependent) TSF rates $1/\tau_{\text{NZ-H}}$ and $1/\tau_{\text{NZ-C}}$ are known.

We now show experimentally, that the addition of trityl does indeed lead to enhanced relaxation of protons and carbons, as well as to $^1\text{H} \leftrightarrow ^{13}\text{C}$ exchange *via* the electron Non-Zeeman reservoir at intermediate fields. We then use a first principles calculation of the (field-dependent) TSF rates τ_{SSI}^{-1} and the experimental relaxation data to determine the (field-independent) heat capacity of the trityl Non-Zeeman reservoir. The latter is found to be larger than predicted by recent Monte Carlo simulations,¹⁸ and we attribute the discrepancy to trityl's known tendency to cluster.^{20,21} Knowledge of the Non-Zeeman heat capacity and the TSF rates enables us to compute the relaxation rates of the three reservoirs over three orders of magnitude in magnetic field, and we find nearly quantitative agreement between the theoretical prediction and experimental proton relaxation data. These findings support a recent derivation of the triple spin flip rate by Wenckebach.^{16,17,22} The observed carbon relaxation is in qualitative agreement with our model, but we find that the direct $^1\text{H}-^{13}\text{C}$ exchange is increased at low fields, and that relaxation at high fields is slower than predicted by the model. As we discuss below, the latter discrepancy

may be accounted for by limited transfer across the diffusion barrier.

EXPERIMENTAL RESULTS

We report longitudinal relaxation and thermal mixing data in neat $1\text{-}^{13}\text{C}$ pyruvic acid (neat PA) and in $1\text{-}^{13}\text{C}$ pyruvic acid doped with 15 mM OX063 (doped PA) for fields between 5 mT and 2 T. We denote the experimentally observed ^1H relaxation time constants for doped PA with $T_{1,\text{H}}^\bullet$, and those for the neat sample with $T_{1,\text{H}}^\circ$. The same notation is used for ^{13}C . All data have been recorded using a fast-field-cycling setup. Details on sample preparation, the setup and our experiments are described in the *Methods* section and additional information is provided in *Supplementary Material*.

Linear field-dependence of radical-induced relaxation

The field-dependence of the proton and carbon relaxation times $T_{1,\text{H}}^\bullet$ and $T_{1,\text{C}}^\bullet$ for doped PA is shown in Fig. 2(a) and (b) respectively, for temperatures between 4.2 K and 40 K.

At low fields, we find a linear increase of T_1^\bullet with field for both nuclei.

For protons, cf. Fig. 2(a), at temperatures up to 20 K, $T_{1,\text{H}}^\bullet$ increases from typically 100 ms at 10 mT to 10 s at 2 T. Below 100 mT, the proton $T_{1,\text{H}}^\bullet$ increases *linearly* with the applied magnetic field. Beyond 100 mT the increase with field persists, but is less than linear. $T_{1,\text{H}}^\bullet$ decreases slightly as the temperature is increased from 4.2 to 20 K. As the temperature is increased further from 20 to 40 K $T_{1,\text{H}}^\bullet$ decreases significantly, which may be associated with methyl-group-induced relaxation^{24–26}.

Our carbon $T_{1,\text{C}}^\bullet$ data in Fig. 2(b) are shown together with data at 1.8 K and higher field strength recorded by Niedbalski, Lumata and co-workers²³. Niedbalski et al. found that their data are well described by a power law $T_1 = CB^\alpha$, with an exponent of $\alpha = 3.1$, indicated by the dashed gray line. Our data at 4.2 K are in good agreement with the 1.8 K data by Niedbalski et al. At the same time, our data show that at low fields the ^{13}C $T_{1,\text{C}}^\bullet$, like the ^1H $T_{1,\text{H}}^\bullet$, depends approximately linearly on the applied magnetic field. The steep increase in ^{13}C $T_{1,\text{C}}^\bullet$, as observed by Niedbalski et al. at 1.8 K, may be attributed to the substantial electron spin polarization P_0 , which leads to a suppression of triple-spin flips. As shown in Fig. 2 (b), a corresponding correction of the observed linear dependence gives a satisfactory description over more than four orders of magnitude in T_1 .

It is instructive to compare the relaxation of both protons and carbons in the presence of trityl to that in neat PA. Relaxation rates of both nuclei, recorded at 4.2 K, are shown for non-degassed neat and doped PA in Figure 2(c). We note three observations: (i) For neat PA,

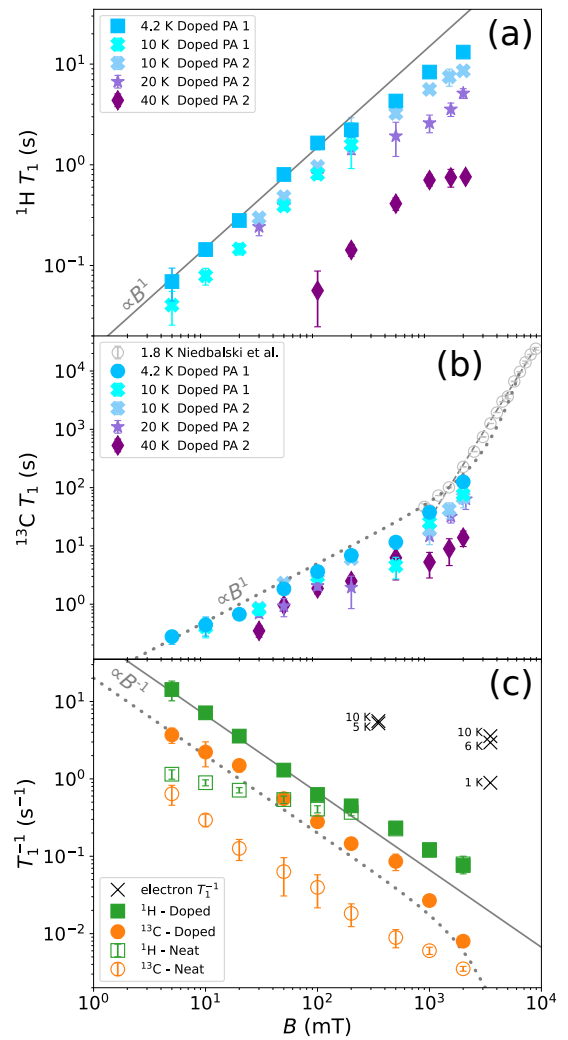


Figure 2. Temperature-dependent relaxation in $1\text{-}^{13}\text{C}$ PA doped with 15 mM trityl (OX063). The data were recorded at fields from 5 to 2000 mT for ^1H (a) and ^{13}C (b). The gray line in (a) is a guide to the eye according to $T_1 = cB^1$ with $c = 15 \text{ s/T}$. The gray 1.8 K data in (b) are reproduced from Ref.²³. The dashed gray line corresponds to a power law with an exponent $\alpha = 3.1$ as reported by Niedbalski, Lumata and co-workers based on measurements at 1.8 K and fields from 0.9 to 9 T. The dotted gray line in (b) is computed using $T_1 = cB/(1 - P_0^2)$, where $c = 50 \text{ s/T}$, and $P_0 = \tanh(\hbar\gamma_S B/(2k_B T))$ is the electron spin polarization. The 4.2 K data from panels (a) and (b) are plotted again as rates in panel (c) (solid symbols), where they are compared to the relaxation rates measured on neat PA (open symbols). The presence of OX063 increases the relaxation rate of carbons throughout the observed field range, and causes faster proton relaxation, up to a field of approximately 200 mT.

the rates $1/T_1^\circ$ of protons and carbons converge at low field, which is expected based on reports of direct low-field thermal mixing in neat PA^{27,28}. This direct exchange, described by $\tau_{\text{H-C}}^{-1}$ in Equations (3) and (4) is negligible for $B > 10 \text{ mT}$ but becomes large as the field approaches zero. (ii) At high fields, the proton rates for

doped and neat PA converge - both materials exhibit similar relaxation times $T_{1,H}^\bullet \approx T_{1,H}^o$ above 500 mT going up to ~ 10 s at 2 T and 4.2 K. This value is consistent with an earlier study²⁸ and linked to the presence of oxygen in non-degassed PA. (iii) The presence of trityl significantly accelerates the relaxation of carbon over the entire field range, and that of protons at fields below 200 mT.

In addition to the nuclear relaxation rates, Fig. 2(c) also shows electron spin-lattice relaxation rates reported by Lumata et al.¹⁹. These indicate an approximately field-independent $T_{1,S}^{-1} \approx 5$ s⁻¹. Note that a significant field-dependence of the electron T_1 is not expected, since trityl relaxes predominantly via oxygen.²⁹

Radical-induced Thermal Mixing

Low-field thermal mixing experiments were carried out on doped PA at 3, 4.2, 10 and 20 K, and on neat PA at 4.2 K. In these experiments the carbon spins are saturated while the proton polarization is allowed to achieve thermal equilibrium at 2 T. The field is then ramped to the mixing field for the duration of the mixing delay. Subsequently the field is ramped back to 2 T, where the ¹³C spin polarization is read out. Further details are given in the *Supplementary Materials*.

In order to quantify the effectiveness of the thermal mixing step we define the thermal mixing efficiency η as the observed signal divided by the thermal equilibrium signal of ¹³C at 2 T. Since the heat capacity of a spin reservoir scales as $\gamma_I^2 N_I$,¹⁴ we can neglect the heat load of the carbon reservoir on the proton reservoir. A thermal mixing efficiency of 100% then implies that the carbon spins attain the spin temperature of the proton spins without any losses and corresponds to the theoretical maximum that can be attained by thermal mixing in the absence of any relaxation.

The dependences of TM efficiency on mixing delay at different fields measured in neat and doped PA at 4.2 K are shown in the left and right panels of Fig. 3, respectively. For neat PA we find thermal mixing is most efficient well below 10 mT, in agreement with a previous study²⁸. We note, however, a limited polarization transfer to carbon in neat PA at fields up to 100 mT, corresponding to a carbon polarization of approximately 15% of its thermal equilibrium value at 2 T. This transfer occurs during the field ramp, and may be associated with the presence of oxygen in the sample. Such a finite polarization transfer at fields above 10 mT has also been observed by Peat et al., provided the sample did contain oxygen²⁸.

For doped PA we also find low field thermal mixing similar to the neat sample up to 5 mT, although η decreases faster for longer mixing delays owing to the radical-enhanced relaxation in the doped sample. The maximum TM efficiency of approximately 40% is observed at 20 mT and a mixing delay of 0.05 s. Between 20 mT and 200 mT well-resolved TM efficiency maxima at increasing mixing times can be observed. The apparent monotoneous increase in TM efficiency at magnetic fields above 200 mT and long mixing delays is due to ¹³C relaxation towards thermal equilibrium with the lattice.

We note that the range of fields where we observe efficient TM, i.e. 20 mT to 200 mT, corresponds to the range where radical-enhanced carbon and proton relaxation rates (Fig. 2) are fairly close to one another. Both effects hint at a coupling of carbon and proton reservoirs in this field range mediated by the added trityl.

THE TRIPLE-SPIN-FLIP RATE AND THE ELECTRON NON-ZEEMAN HEAT CAPACITY

We now calculate the field-dependent TSF rates for carbons and protons, and use the result to determine the heat capacity of the electron Non-Zeeman reservoir.

The Triple-Spin-Flip Rate

In the high-temperature approximation, the change in electron non-Zeeman energy E_{NZ} due to exchange with some nuclear reservoir via TSFs is¹⁷

$$\left(\frac{\partial E_{NZ}}{\partial t} \right)_{SSI} = \frac{C_{NZ}}{\tau_{NZ-I}} (\beta_{NZ} - \beta_I) \quad (6)$$

Note that TSFs can also exchange electron Zeeman energy with nuclear reservoirs, a process known as the cross effect. The heat capacity of the corresponding electron reservoir is given by the second moment of the inhomogeneous EPR line, which is substantially narrower than the spin-spin spectrum for the fields investigated in this study. We therefore consider only thermal mixing with the electron non-Zeeman reservoir.

An expression for the left-hand side of equation (6) has been given by Wenckebach^{17,30}, and the matrix elements therein have recently been evaluated explicitly²². As detailed in the Supplementary Material, Eq. (6) may be solved for the triple spin flip rate, and the result for thermal mixing is

$$\frac{1}{\tau_{NZ-I}} = \frac{C_I}{C_{NZ}} \frac{\pi^2}{5} \left(\frac{\mu_0}{4\pi} \hbar \gamma_I \gamma_S \right)^2 \frac{N_S}{r_{ba}^3} \cdot \int_{-\omega_{0I}}^{\omega_{0I}} d\Delta \int_{-\infty}^{\infty} d\omega g_i(\omega) g_i(\omega - \Delta) \frac{(\omega_{0I}^2 - \Delta^2)^{3/2}}{\omega_{0I}^3} g_D \left(\sqrt{\omega_{0I}^2 - \Delta^2} \right). \quad (7)$$

The TSF rate thus depends on the number density of

electron spins N_S , the distance between the electron and

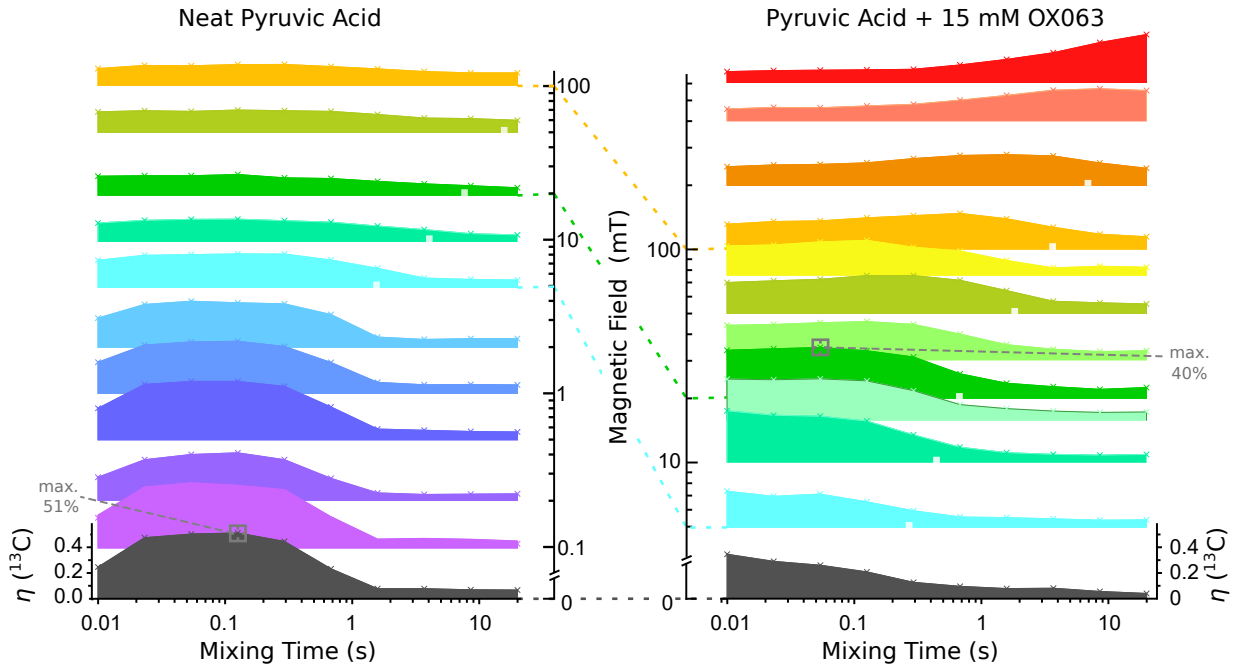


Figure 3. Thermal mixing in neat (left) and doped (right) PA at 4.2 K for fields from zero up to 200 mT and 600 mT, respectively. All data were normalized to the thermal equilibrium ^{13}C signal at 4.2 K and 2 T (see supporting information), with the scale indicated for the respective zero-field data (lower left/right). TM efficiency is shown as a function of mixing delay. The maximum (indicated by gray squares) is 51% at 0 mT for neat PA and 40% at 20 mT for doped PA. The increase of signal intensity at the highest magnetic fields and long mixing delays is due to a build-up of polarization of ^{13}C nuclei in high magnetic field with ^{13}C T_1 (indicated, where available, by white squares in the respective datasets). The finite duration of the magnetic field ramp leads to a degree of TM before and after the evolution delay, hence a finite TM efficiency for very short mixing delays. For a ramp down to zero field, the ramp time spent below 200 mT is of the order of 100 ms.

the nearest nuclear spins outside the diffusion barrier r_{ba} , the spectrum of electron spin-spin interactions $g_D(\omega)$ and the inhomogeneous EPR lineshape $g_i(\omega)$. The number density is known from the trityl concentration, and we set r_{ba} to 0.7 nm.

Monte Carlo simulations¹⁸ yield a spectrum of electron spin-spin interactions that can be described by the normalized product of a Gaussian with a Lorentzian, with linewidths for our system of $\Delta_G/2\pi = 8.48$ MHz and $\Delta_L/2\pi = 1.18$ MHz. Note that the second moment M_2 of this spectrum corresponds to a dipolar frequency of only $\sqrt{M_2}/2\pi = 2.7$ MHz, with a corresponding Non-Zeeman heat capacity of 0.12 J rad/(s mL).

For the inhomogeneous EPR line we assume a Gaussian with linewidths interpolated from EPR data reported by Lumata et al.¹⁹, further details are given in the supplementary material.

The resulting field-dependent TSF rates for hydrogen $\tau_{\text{NZ-H}}^{-1}$ calculated with the aforementioned Monte Carlo-based parameters are shown in Fig. 4(b), along with the hydrogen relaxation rate due to trityl, $\Delta T_{1,\text{H}}^{-1} = T_{1,\text{H}}^{\bullet-1} - T_{1,\text{H}}^{\circ-1}$. The TSF rate $\tau_{\text{NZ-H}}^{-1}$ exceeds the electron spin-lattice relaxation rate $T_{1,\text{S}}^{-1}$ for fields up to 1 T. Furthermore, we show in Fig. 4(a) that the hydrogen heat capacity exceeds that of the electron NZ reservoir throughout our experimental range, $C_{\text{H}} \gg C_{\text{NZ}}$ for the

Monte Carlo model. Under these conditions, known as *fast thermal mixing* the NZ reservoir equilibrates very rapidly with the proton reservoir, and we have $\beta_{\text{NZ}} = \beta_{\text{H}}$. Disregarding carbon one can deduce from Equations (3) and (5) that the increase in proton relaxation then is

$$\Delta T_{1,\text{H}}^{-1} = \frac{C_{\text{NZ}}}{C_{\text{H}}} T_{1,\text{S}}^{-1}. \quad (8)$$

Since we assume a field-independent $T_{1,\text{S}}^{-1} \approx 5\text{s}^{-1}$, (8) predicts an inversely quadratic field dependence of $\Delta T_{1,\text{H}}^{-1}$. This dependence is shown as dashed green line in Fig. 4(b), where we assume $C_{\text{NZ}} = 0.12\text{ J rad/(s mL)}$ as predicted by the Monte Carlo simulations¹⁸.

The Electron Non-Zeeman Heat Capacity

One can see from Eq. (8) that $\Delta T_{1,\text{H}}^{-1}$ is limited by the field-independent heat capacity of the Non-Zeeman reservoir. Experimentally, the additional relaxation due to trityl follows the predicted quadratic field dependence above 20 mT, but the experimental relaxation rates are approximately an order of magnitude larger than the Monte Carlo based prediction.

A good match between Eq. (8) and the experimental data is obtained when we assume an electron Non-

Zeeman capacity of 23 J rad/(s mL) . The larger Non-Zeeman heat capacity has to be matched by a corresponding increase in the second moment of the electron spin-spin spectrum. We therefore approximate the spin-spin spectrum by a Gaussian g_D with a dipolar frequency of $\sqrt{M_2}/2\pi = 38 \text{ MHz}$.

A larger second moment is plausible, given the reported propensity of trityl radicals to cluster^{20,21}, and the fact that just the dipolar frequency for just two radicals touching is already 54 MHz. The precise radical distribution and corresponding EPR spin-spin spectrum cannot be determined from our data, nor are they critical to our analysis. As detailed in the *Supplementary Material*, the observed second moment is readily generated by different spin-spin spectra yielding similar TSF rates, and we

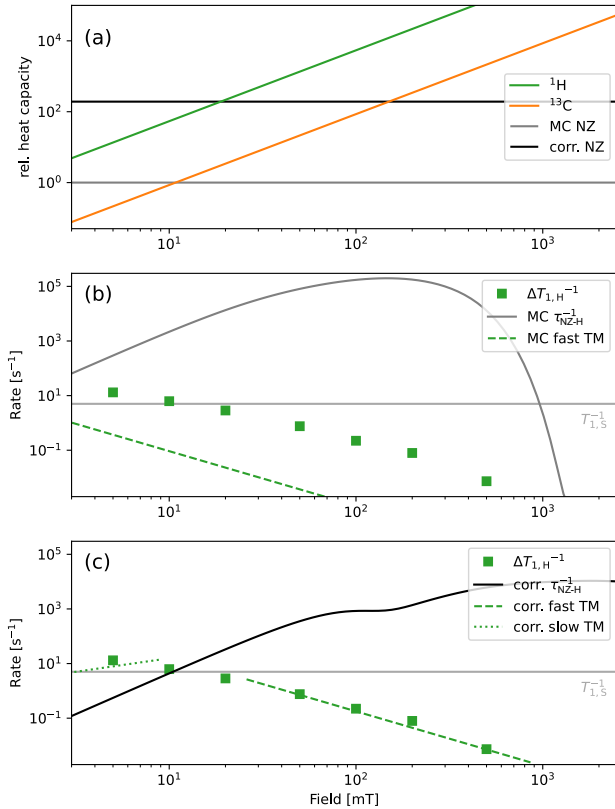


Figure 4. (a) Reservoir heat capacities relative to the NZ reservoir based on Monte Carlo simulations ($\sqrt{M_2}/2\pi = 2.7 \text{ MHz}$)¹⁸ C_i/C_{NZ} . Nuclear reservoirs grow quadratically with magnetic field, whereas NZ in Monte Carlo and corrected model are field-independent. (b) The proton TSF rate (solid gray line) as calculated with the Monte Carlo spin-spin spectrum predicts due to fast thermal mixing (dashed line according to Eq. 8) that underestimates the observed increase in proton relaxation rate $\Delta T_{1,H}$ by more than one order of magnitude. (c) The corrected model with $\sqrt{M_2}/2\pi = 38 \text{ MHz}$ yields a TSF rate (solid black line) that predicts fast thermal mixing (dashed line) for $30 \text{ mT} < B < 1 \text{ T}$ and slow thermal mixing (dotted line, Eq. 9) for $B \ll 10 \text{ mT}$, both quantitatively in agreement with measured increase in the proton relaxation rate $\Delta T_{1,H}$.

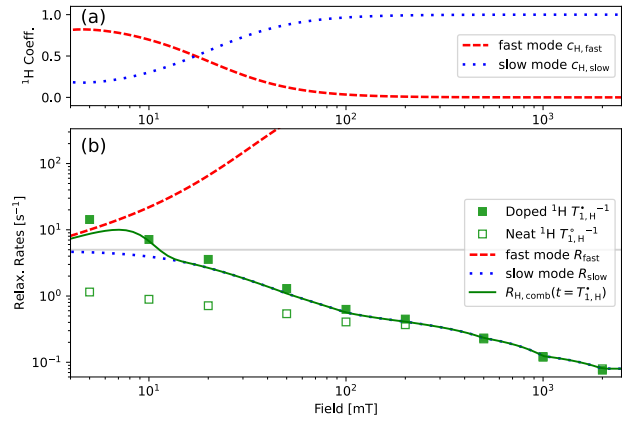


Figure 5. Field-dependent proton relaxation described by bi-modal relaxation for two coupled reservoirs, protons and electron NZ. (a) Proton coefficients for the fast and slow mode relaxation in dependence on field. (b) Corresponding fast and slow mode relaxation rates compared to experimental data. Also shown is the coefficient-weighted average relaxation rate $R_{\text{H,comb}}(t = T_{1,H})$ predicted for protons at the time measured experimentally.

choose one close to an experimental EPR spectrum.¹⁹

The triple spin flip rate for protons, recalculated for the larger heat capacity of the spin spin spectrum g_D , is compared to the experimental data in Fig. 4(c). As can be seen, the conditions for fast thermal mixing is still fulfilled above 20 mT, where the inversely quadratic field dependence is observed.

At lowest fields the corrected NZ heat capacity exceeds that of the proton reservoir, cf. Fig. 4(a), and the corrected TSF rate is smaller than the the electron spin-lattice relaxation, cf. Fig. 4(c). Under these conditions the NZ reservoir's temperature remains at lattice temperature ($\beta_{\text{NZ}} = 0$) which is the limiting case of so-called *slow thermal mixing*. Disregarding carbon, one can then deduce from (3) and (5)

$$\Delta T_{1,H}^{-1} = \frac{C_{\text{NZ}}}{C_{\text{H}}} \tau_{\text{NZ-H}}^{-1}. \quad (9)$$

The expected $\Delta T_{1,H}^{-1}$ according to (9) in that lower field range is indicated by the dotted green line in Fig. 4(c). While sufficient low field data points are lacking to confirm the expected linear dependence ($C_{\text{H}}^{-1} \cdot \tau_{\text{NZ-H}}^{-1} \propto B^{-2} \cdot B^3 = B^1$), quantitatively the agreement at 5 mT is satisfactory.

Relaxation Model and Data

We now use the heat capacities and the TSF rates as determined in the previous section, as well as the nuclear relaxation rates of the neat sample, to model the experimental data on doped PA quantitatively throughout the measured field range.

The carbon Zeeman reservoir is $C_H/C_C \approx 64$ times smaller than the proton Zeeman reservoir. For fields up to approximately 500 mT, we furthermore have $\tau_{\text{NZ}-\text{C}}^{-1} < \tau_{\text{NZ}-\text{H}}^{-1}$, so that the influence of the carbon reservoir on the Non-Zeeman reservoir can be ignored.

Rewriting (3) and (5) in matrix form without the carbon contributions yields:

$$\frac{\delta}{\delta t} \begin{pmatrix} \beta_H \\ \beta_{\text{NZ}} \end{pmatrix} = \dot{\vec{\beta}} = \begin{pmatrix} -A & C \\ D & -B \end{pmatrix} \cdot \vec{\beta} \quad (10)$$

with the relaxation matrix entries $A = T_{1,\text{H}}^{\circ}{}^{-1} + C_{\text{NZ}}/C_{\text{H}}$, $\tau_{\text{NZ}-\text{H}}^{-1}$, $B = \tau_{\text{NZ}-\text{H}}^{-1} + T_{1,\text{S}}^{-1}$, $C = \tau_{\text{NZ}-\text{H}}^{-1} C_{\text{NZ}}/C_{\text{H}}$ and $D = \tau_{\text{NZ}-\text{H}}^{-1}$.

The solution of the eigenvalue problem (10) is given by $\vec{\beta}(t) = \sum_{i=1}^2 a_i \vec{v}_i \exp(\lambda_i t)$ with the eigenvalues λ_i and eigenvectors \vec{v}_i to the relaxation matrix. The coefficients a_i then are given by the initial conditions. In our experiments, the Non-Zeeman reservoir is initially at the lattice temperature, i.e., $\beta_{\text{NZ}}(t=0) = 0$, while the inverse proton temperature is finite.

As detailed in the *Supplementary Material*, the evolution of the two reservoirs can then be written as

$$\vec{c}(t) = \beta_H(0) (\vec{c}_{\text{fast}} \cdot e^{-R_{\text{fast}} t} + \vec{c}_{\text{slow}} \cdot e^{-R_{\text{slow}} t}), \quad (11)$$

where the coefficients are

$$\vec{c}_{\text{fast/slow}} = \begin{pmatrix} c_{\text{H,fast/slow}} \\ c_{\text{NZ,fast/slow}} \end{pmatrix} = \begin{pmatrix} \frac{A-B \pm \sqrt{(A-B)^2 + 4CD}}{2\sqrt{(A-B)^2 + 4CD}} \\ \mp \frac{2D}{2\sqrt{(A-B)^2 + 4CD}} \end{pmatrix}, \quad (12)$$

and the relaxation rates are the eigenvalues of the relaxation matrix,

$$R_{\text{fast/slow}} = -\lambda_{1,2} = \frac{1}{2} (A + B \pm \sqrt{(A - B)^2 + 4CD}). \quad (13)$$

The fast mode balances the Non-Zeeman reservoir and the proton reservoir inverse temperatures, whereas the slow mode equilibrates the combined two reservoirs with the lattice.

The field-dependent coefficients and the relaxation rates of the two modes are shown in Fig. 5(a) and (b), respectively. In Fig. 5(b), we also show the experimentally observed ^1H relaxation rates for neat and doped PA. At the lowest observed field of 5 mT, the proton relaxation is dominated by the fast mode, which corresponds to a flow of heat from the electron Non-Zeeman reservoir to the proton Zeeman reservoir. As the field is increased, the proton Zeeman heat capacity increases, and so the influence of the electron Non-Zeeman reservoir on its evolution decreases. In the intermediate regime, the evolution is biexponential, and the observed proton relaxation rates fall between the fast and the slow mode.

Since the experimental data do not warrant an extraction of two coefficients and two decay rates, we compare the experimental data with the effective relaxation rate,

evaluated at the observed proton $T_{1,\text{H}}^{\bullet}$, details are given in the SI. As can be seen in Fig. 5, our model quantitatively describes the observed proton relaxation rates quite well.

In order to describe ^{13}C relaxation, we now include the ^{13}C reservoir and calculate the relaxation rates through a numerical diagonalization of the relaxation matrix (3)-(5) at each field. The time evolution of the three reservoirs may then be written in general as

$$\vec{\beta}(t) = \begin{pmatrix} \beta_H(t) \\ \beta_C(t) \\ \beta_{\text{NZ}}(t) \end{pmatrix} = \sum_{i=1}^3 a_i \vec{v}_i \exp(-R_i t), \quad (14)$$

where the relaxation rates R_i are again given by the field-dependent eigenvalues ($\lambda_i = -R_i$) of the relaxation matrix, the \vec{v}_i are its field-dependent eigenvectors, and the a_i are set by the initial conditions.

In Fig. 6(a) we compare the calculated TSF rate for carbon τ_{SSC}^{-1} to that for protons τ_{SSH}^{-1} . The rates scale with the heat capacity of the respective nuclear reservoirs, and so the TSF rate for carbon is substantially smaller than that for protons. Their field dependences are shifted relatively, e.g., the peak rate field, by a factor $\frac{\gamma_{\text{H}}}{\gamma_{\text{C}}} \approx$ due to limits of the first integral in (7).

As expected, the presence of the carbon reservoir does not affect the resulting proton relaxation (full green line in Fig. 6 (b)).

The solution for the expected carbon rate (full orange line in Fig. 6 (b)), however, does not describe the measured carbon rates well. At fields up to 20 mT, the predicted relaxation rates are smaller than the ones observed in experiment. At fields above 50 mT, the predicted relaxation rates are larger than the ones observed in experiment. Note that in the latter regime, the predicted ^{13}C relaxation rates equal the ^1H relaxation rates due to the tight coupling of both nuclear reservoirs to the electron NZ reservoir.

The discrepancy at low fields may be attributed to direct thermal mixing between the ^1H and ^{13}C reservoirs. The rate for this process, denoted by $\tau_{\text{H}-\text{C}}$ in (3) & (4), is negligible above 20 mT but becomes significant at lower fields.²⁸ Note that this direct mixing process causes the thermal mixing shown in the left panel of Fig. 3 as well as the convergence of the experimental carbon and proton relaxation rates at low fields in neat PA. Therefore, in neat PA below 20 mT, $\tau_{\text{H}-\text{C}}^{-1}$ corresponds to the experimentally observed carbon relaxation rate.

We find that the low-field relaxation rates of ^{13}C in doped PA are well described by $5 \cdot T_{1,\text{C}}^{\circ}{}^{-1}$, i.e. the direct proton-carbon relaxation rates scale with the neat rates, but are accelerated 5-fold. We attribute this increase to line-broadening due to the presence of trityl in doped PA.

The discrepancy observed at fields above 50 mT may be attributed to spin diffusion across the diffusion barrier. In the model, the protons are in the fast thermal mixing limit, and so the proton reservoir sets the temperature of the Non-Zeeman reservoir. As the field is increased, the carbon reservoir increasingly couples to the NZ reservoir,

and so the model predicts the same spin temperatures and hence relaxation rates for both protons and carbons. However, only a minute portion of nuclear spins in the radical vicinity, referred to as *core spins*, are in direct exchange with the electron NZ reservoir as described by (3)-(5). The close proximity to the radicals causes a shift in the resonance frequency of the core spins, which in turn impedes diffusion to the bulk spins. As shown recently by Stern et al.³¹, the core spins do nonetheless exchange polarization with the bulk spins. This exchange may again be modelled with two coupled reservoirs that represent the core and bulk spins, respectively. The diffusion barrier limits the exchange of Zeeman energy between these reservoirs, and only the bulk spins are visible in the NMR spectrum.

The energy flow across the barrier is frequently attributed to dipolar interactions³⁴, and it is conceivable that the coupling of the two reservoirs is field-dependent, since more Zeeman energy has to be transferred across the barrier at higher fields. As detailed in the Supplementary Material, the relaxation model (3)-(5) may be extended with a second carbon reservoir and a field-dependent carbon core-bulk time constant of 33 s/T. This rather heuristic model leads to a satisfactory description of the experimental data, as shown in Fig. 6.

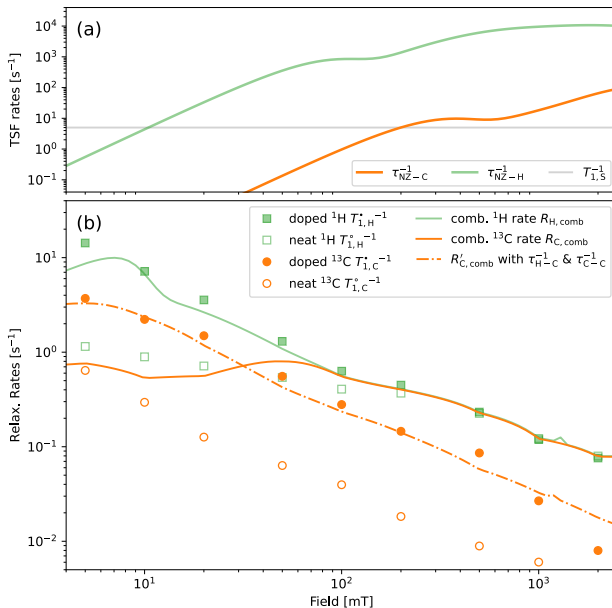


Figure 6. Carbon relaxation described by three-reservoir relaxation. (a) Comparison of calculated TSFs for carbon and protons. (b) The resulting coefficient-weighted average relaxation rate for protons $R_{H,comb}(t = T_{1,H}^•)$ is not affected by inclusion of the carbon reservoir. The calculated rate for carbon $R_{C,comb}(t = T_{1,C}^•)$ is slower than experimental rates $T_{1,C}^•$ $^{-1}$ for fields up to 20 mT and faster above. Between 100 mT and 1 T the relatively high TSF rate for carbon causes the calculated rate to be tied to the proton relaxation rate. Taking into account direct low-field mixing with protons and carbon spin-diffusion, the ¹³C data are well described (dash-dot line), for details see text.

DISCUSSION

The relaxation data reported here explain the success of our bullet-DNP experiments^{9,10}. Earlier work at fields above 1 T indicates a scaling of relaxation rates with field according to $T_1 \sim B^3$ ¹⁹ and, consequentially, very fast relaxation at low fields. Conversely, our data show that below 1 Tesla the relaxation rates scale only linearly with the applied field. The relaxation rates are acceptable also for transferring hyperpolarized protons, provided that the sample temperature does not exceed 20 K.

The presence of trityl leads to a thermal contact between the proton and carbon reservoirs, that is directly evident at fields up to 500 mT from the reported mixing experiments. In this regime, carbon and proton spins exchange energy on a time scale that is faster or similar to the experimental proton relaxation rate. At fields above 500 mT, carbon and proton spins exchange energy on a time scale that is slower than the experimental proton relaxation rate. In this regime, we therefore do not observe a maximum in thermal mixing efficiency. Nonetheless, the carbon spins are coupled to the proton spins via the Non-Zeeman reservoir, and we attribute the increased carbon relaxation rate in doped PA to this coupling.

While protons cannot couple to the electron spins of trityl via the cross-effect, the cut-off frequency or field up to which thermal mixing occurs depends on the details of the spin-spin spectrum. The second moment of the spin-spin spectrum sets a lower bound for this cut-off. For a homogeneous distribution of radicals as it is obtained from Monte Carlo simulations, the proton TSF rate decreases sharply above 1 T. In order to model our data, we need to assume a broader spin-spin spectrum with a higher second moment, which increases the cut-off field for a given nuclear species. This finding may support the attribution of ¹H DNP at a field of 7 T to thermal mixing in DNP substrates with substantial trityl concentrations²⁰.

The experimentally observed carbon relaxation rates at fields above 50 mT are substantially smaller than those predicted by our model. One possibility is that this reduction arises from slow carbon spin diffusion. The carbon line in 1-¹³C PA has a significant contribution from chemical shift anisotropy³², and one may expect spin diffusion to limit the overall ¹³C relaxation as the field, and thereby the carbon linewidth, is increased³³. However, at the fields investigated in this study, the carbon line is strongly dominated by dipolar interactions, so that this approach cannot account for the field-dependence of the observed carbon T_1 .

In the favoured alternative explanation of the observed carbon relaxation rates, the diffusion barrier separates the carbon spins into invisible core nuclei inside the barrier, and visible bulk nuclei outside the barrier. The diffusion among the bulk nuclei is fast, and so the carbon relaxation rate is limited by the coupling between core and bulk nuclei. Convincing evidence for this mechanism

has been presented recently,³¹ although no experimental studies of the field-dependence of this coupling have been presented to date.

CONCLUSION

We have shown that the proton and carbon low-temperature low-field nuclear spin-lattice relaxation rates of pyruvic acid doped with trityl scale linearly with the applied magnetic field, with no significant temperature dependence up to 20 K. The data are well described by a spin temperature model in which both the proton and carbon Zeeman reservoirs couple to the electron non-Zeeman reservoir, and all reservoirs are coupled to the lattice. The evolution is then governed by the couplings between the reservoirs and their heat capacities. The coupling between the electron non-Zeeman reservoir and the nuclear reservoirs is due to triple-spin-flips. The triple-spin-flip rates are calculated from first principles, using only the density of the involved spins, experimental EPR data, and a recent Monte-Carlo based estimate of the electron spin-spin interaction spectrum. In order to account for the nuclear relaxation data, we have to assume an electron spin-spin interaction with a larger second moment than that derived from Monte-Carlo simulations. The difference is attributed to a degree of radical aggregation. With this correction, we find that the formalism for triple-spin-flip rates derived by Wenckebach is capable of describing the observed proton relaxation rates nearly quantitatively over two orders of magnitude in field, and two orders of magnitude in relaxation time, without any other adjustable parameters. The model does not quantitatively predict the observed carbon relaxation rates. At fields below 50 mT, trityl is found to accelerate direct proton-carbon mixing. At fields above 50 mT, the carbon relaxation rates are inversely proportional to the applied field, which we provisionally attribute to field-dependent energy transfer across the diffusion barrier.

MATERIALS AND METHODS

Sample preparation and loading

Neat 1-¹³C-pyruvic acid was purchased from Cortec-Net, FR, and OX063 trityl radical was purchased from Oxford Instruments, UK. Experiments on neat pyruvic acid were carried out on a single sample, referred to as Neat PA, during a single session. Two experimental sessions were required to record data on 15 mM OX063 in 1-¹³C pyruvic acid. A fresh sample was prepared for each session, and we refer to these samples as Doped PA 1 and Doped PA 2 in this manuscript. All samples were used without degassing.

For each experiment the corresponding solution was pipetted into either a glass tube and sealed with PTFE tape, or into a PTFE sample cup and closed using a lid

with a small hole in its rotation symmetry axis to allow for the pressure equilibration. The sealed tube or the sample cup was inserted into the NMR coil. The samples were flash-frozen by immersion of the NMR probe into the cold variable temperature insert of the magnet.

Fast field cycling (FFC) apparatus

Experiments were carried out using a fast field cycling (FFC) apparatus (Cryogenic Ltd) at the University of Nottingham, UK. The system comprises a low-inductance superconducting magnet and a fast-ramping power supply. The magnet houses a sample flow cryostat and a variable temperature insert (VTI). Stable temperatures in the range of 3 to 300 K and magnetic fields from 0 to 2.5 T are achieved. The magnetic field changes were performed at a rate of 4 T/s, and the absolute error of the magnetic field strength is 2 mT. A Tecmag Apollo NMR spectrometer (Tecmag, TX) with a home-written visual basic extension enables a control of the magnetic field strength from within the NMR pulse sequence. Here we used a home/built NMR probe with a solenoid tuned to a frequency of 21.6 MHz. This frequency corresponds to a resonant magnetic field B_{res} of approximately 0.5 and 2 Tesla for proton and carbon spins, respectively. More detailed descriptions of this setup can be found elsewhere^{28,36}.

FFC-NMR Experiments and Analysis

For T_1 measurements two pulse sequences were used. For low evolution fields ($B_{\text{evo}} < 0.2$ T for ¹H, $B_{\text{evo}} < 0.5$ T for ¹³C) the polarization from a simple saturation recovery experiment would be too small. Here a *polarization decay* sequence was used where nuclear spins are first saturated at B_{res} to ensure reproducibility, and then polarized for 70 s at polarizing magnetic field of 2 T. In the next stage this polarization relaxes over a time t_{evo} to the new thermal equilibrium at the lower evolution field B_{evo} , before the field is ramped up again to the resonant field B_{res} and the signal is read out.

For higher field strengths a *saturation recovery* sequence was used, in which the polarization step is skipped and the field is shifted to B_{evo} right after the saturation step. The polarization is allowed to recover for a variable time at a set field (stage III), and the magnetic field is ramped up to the detection field where the signal is read out (stage IV). The relaxation time $T_1(B_{\text{evo}})$ is obtained by applying an single exponential fit to the integrated spectral intensities S for increasing evolution times t_{evo} as $S(t_{\text{evo}}) = A \cdot \exp(-t_{\text{evo}}/T_1) + S_0$, where S_0 should correspond to equilibrium polarization at B_{evo} and A to either the excess polarization $S_0(2\text{T}) - S_0(B_{\text{evo}})$ (polarization decay) or $-S_0$ (saturation recovery).

For **thermal mixing experiments** proton polarization was allowed to reach thermal equilibrium at the ¹³C reso-

nance field of 2 T, while the carbon spins are saturated. Then the magnetic field is lowered to the mixing field B_{mix} where no pulses are applied. At sufficiently low B_{mix} , low-field thermal mixing leads to a transfer of spin polarization from proton to carbon spins. For higher mixing fields thermal mixing becomes less efficient. For very long mixing delays, $t_{\text{mix}} \approx T_{1,C}(B_{\text{mix}})$, an increase in carbon signal is observed that, however, is due to carbon spin-lattice relaxation to thermal equilibrium at the mixing field. For observation after t_{mix} the is ramped back up to the ^{13}C resonance field and the NMR signal is read out.

For **data processing and analysis** the recorded FIDs were left-shifted by 10 points and Fourier transformed, the NMR spectra were phased with zero-order correction and the signals were integrated with a 10 kHz integration window using the NTNMR software of the Tecmag spectrometer.

The integrals were further processed and analysed using Python and Origin Pro.

ACKNOWLEDGMENTS

We thank Tom Wenckebach for numerous discussions and assistance with the relaxation model. We thank Lloyd Lumata for discussions and for providing the OX063 low-field EPR spectrum and the high-field ^{13}C T_1 data, and David Gadian for discussions and help with experiments. This work has been supported by EPSRC (EP/R031959/1) and by the “Impuls- und Vernetzungsfonds of the Helmholtz-Association” under grant VH-NG-1432. This project has received funding from the European Research Council (ERC) under the European Union’s Horizon 2020 research and innovation programme (grant agreement No 951459).

* hana.kourilova@kit.edu

† michael.jurkutat@kit.edu

‡ benno.meier@kit.edu

¹ J. H. Ardenkjær-Larsen, B. Fridlund, A. Gram, G. Hansson, L. Hansson, M. H. Lerche, R. Servin, M. Thaning, and K. Golman, *Proceedings of the National Academy of Sciences* **100**, 10158 (2003).

² J. H. Ardenkjær-Larsen, *Handbook of High Field Dynamic Nuclear Polarization* , 239 (2019).

³ W. Köckenberger, “Dissolution dynamic nuclear polarization,” in *eMagRes*, eMagRes (John Wiley & Sons, Ltd, 2014) pp. 161–170.

⁴ D. Kurzbach and S. Jannin, “Dissolution dynamic nuclear polarization methodology and instrumentation,” in *eMagRes* (American Cancer Society, 2018) pp. 117–132.

⁵ S. J. Nelson, J. Kurhanewicz, D. B. Vigneron, P. E. Z. Larson, A. L. Harzstark, M. Ferrone, M. van Criekinge, J. W. Chang, R. Bok, I. Park, G. Reed, L. Carvajal, E. J. Small, P. Munster, V. K. Weinberg, J. H. Ardenkjær-Larsen, A. P. Chen, R. E. Hurd, L.-I. Odegardstuen, F. J. Robb, J. Tropp, and J. A. Murray, *Science Translational Medicine* **5**, 198ra108 (2013).

⁶ Z. J. Wang, M. A. Ohlinger, P. E. Z. Larson, J. W. Gordon, R. A. Bok, J. Slater, J. E. Villanueva-Meyer, C. P. Hess, J. Kurhanewicz, and D. B. Vigneron, *Radiology* **291**, 273 (2019).

⁷ F. A. Gallagher, R. Woitek, M. A. McLean, A. B. Gill, R. M. Garcia, E. Provenzano, F. Riemer, J. Kaggie, A. Chhabra, S. Ursprung, J. T. Grist, C. J. Daniels, F. Zaccagna, M.-C. Laurent, M. Locke, S. Hilborne, A. Frary, T. Torheim, C. Boursnell, A. Schiller, I. Patterson, R. Slough, B. Carmo, J. Kane, H. Biggs, E. Harrison, S. S. Deen, A. Patterson, T. Lanz, Z. Kingsbury, M. Ross, B. Basu, R. Baird, D. J. Lomas, E. Sala, J. Wason, O. M. Rueda, S.-F. Chin, I. B. Wilkinson, M. J. Graves, J. E. Abraham, F. J. Gilbert, C. Caldas, and K. M. Brindle, *Proceedings of the National Academy of Sciences* **117**, 2092 (2020).

⁸ R. Woitek, M. A. McLean, S. Ursprung, O. M. Rueda, R. M. Garcia, M. J. Locke, L. Beer, G. Baxter, L. Rundo,

E. Provenzano, J. Kaggie, A. Patterson, A. Frary, J. Field-Rayner, V. Papalouka, J. Kane, A. J. Benjamin, A. B. Gill, A. N. Priest, D. Y. Lewis, R. Russell, A. Grimmer, B. White, B. Latimer-Bowman, I. Patterson, A. Schiller, B. Carmo, R. Slough, T. Lanz, J. Wason, R. F. Schulte, S.-F. Chin, M. J. Graves, F. J. Gilbert, J. E. Abraham, C. Caldas, K. M. Brindle, E. Sala, and F. A. Gallagher, *Cancer Research* **81**, 6004 (2021).

⁹ K. Kouřil, H. Kouřilová, S. Bartram, M. H. Levitt, and B. Meier, *Nature Communications* **10**, 1733 (2019).

¹⁰ K. Kouřil, M. Gramberg, M. Jurkutat, H. Kouřilová, and B. Meier, *Magnetic Resonance* **2**, 815 (2021).

¹¹ G. Olsen, E. Markhasin, O. Szekely, C. Bretschneider, and L. Frydman, *Journal of Magnetic Resonance* **264**, 49 (2016).

¹² B. Provotorov, *Sov. Phys. JETP* **15** (1962) **15**, 611 (1962).

¹³ B. Provotorov, *Sov. Phys. JETP* **14** (1962) **14**, 1126 (1961).

¹⁴ M. Goldman, *Spin Temperature and Nuclear Magnetic Resonance in Solids* (Oxford University Press, 1970).

¹⁵ W. Wenckebach, *Essentials of Dynamic Nuclear Polarization* (Spindrift Publications, 2016).

¹⁶ W. Wenckebach, *Journal of Magnetic Resonance* **299**, 124 (2019).

¹⁷ W. Wenckebach, *Journal of Magnetic Resonance* **299**, 151 (2019).

¹⁸ W. T. Wenckebach and Y. Quan, *Journal of Magnetic Resonance* **326**, 106948 (2021).

¹⁹ L. Lumata, Z. Kovacs, A. D. Sherry, C. Malloy, S. Hill, J. van Tol, L. Yu, L. Song, and M. E. Merritt, *Phys. Chem. Chem. Phys.* **15**, 9800 (2013).

²⁰ A. Equbal, Y. Li, T. Tabassum, and S. Han, *The Journal of Physical Chemistry Letters* **11**, 3718 (2020).

²¹ I. Marin-Montesinos, J. C. Paniagua, M. Vilaseca, A. Urizbereia, F. Luis, M. Feliz, F. Lin, S. V. Doorslaer, and M. Pons, *Physical Chemistry Chemical Physics* **17**, 5785 (2015).

²² W. T. Wenckebach, *Applied Magnetic Resonance* **52**, 731 (2021).

²³ P. Niedbalski, Q. Wang, C. Parish, F. Khashami, A. Kiswandhi, and L. Lumata, *The Journal of Physical*

Chemistry B **122**, 1898 (2018).

²⁴ L. Latanowicz, Concepts in Magnetic Resonance Part A **27A**, 38 (2005).

²⁵ A. Horsewill, Progress in Nuclear Magnetic Resonance Spectroscopy **35**, 359 (1999).

²⁶ B. Meier, Magnetic Resonance in Chemistry **56**, 610 (2018).

²⁷ M. L. Hirsch, N. Kalechofsky, A. Belzer, M. Rosay, and J. G. Kempf, Journal of the American Chemical Society **137**, 8428 (2015).

²⁸ D. T. Peat, M. L. Hirsch, D. G. Gadian, A. J. Horsewill, J. R. Owers-Bradley, and J. G. Kempf, Physical Chemistry Chemical Physics **18**, 19173 (2016).

²⁹ C. Hess, J. Herick, A. Berlin, W. Meyer, and G. Reicherz, Nuclear Instruments and Methods in Physics Research Section A: Accelerators, Spectrometers, Detectors and Associated Equipment **694**, 69 (2012).

³⁰ W. Wenckebach, A. Capozzi, S. Patel, and J. Ardenkjær-Larsen, Journal of Magnetic Resonance **327**, 106982 (2021).

³¹ Q. Stern, S. F. Cousin, F. Mentink-Vigier, A. C. Pinon, S. J. Elliott, O. Cala, and S. Jannin, Science Advances **7**, 11 (2021).

³² S. Macholl, H. Jóhannesson, and J. H. Ardenkjær-Larsen, Phys. Chem. Chem. Phys. **12**, 5804 (2010).

³³ Y. Wang and K. Takeda, New Journal of Physics **23**, 073015 (2021).

³⁴ G. B. Furman, S. D. Goren, V. M. Meerovich, and V. L. Sokolovsky, Applied Magnetic Resonance **52**, 781 (2021).

³⁵ J. M. Steiner, P. Hautle, and W. T. Wenckebach, Journal of Magnetic Resonance **311**, 107099 (2021).

³⁶ A. J. Horsewill and Q. Xue, Phys. Chem. Chem. Phys. **4**, 5475 (2002).